A human in vitro model of Duchenne muscular dystrophy muscle formation and contractility

Alexander P. Nesmith,[1] Matthew A. Wagner,[1] Francesco S. Pasqualini,[1] Blakely B. O'Connor,[1] Mark J. Pincus,[2] Paul R. August,[2] and Kevin Kit Parker[1]

[1]Disease Biophysics Group, Wyss Institute for Biologically Inspired Engineering and Harvard John A. Paulson School of Engineering and Applied Sciences, Harvard University, Cambridge, MA 02138
[2]Sanofi U.S.-Tucson Innovation Center, Oro Valley, AZ 85755

Tongue weakness, like all weakness in Duchenne muscular dystrophy (DMD), occurs as a result of contraction-induced muscle damage and deficient muscular repair. Although membrane fragility is known to potentiate injury in DMD, whether muscle stem cells are implicated in deficient muscular repair remains unclear. We hypothesized that DMD myoblasts are less sensitive to cues in the extracellular matrix designed to potentiate structure–function relationships of healthy muscle. To test this hypothesis, we drew inspiration from the tongue and engineered contractile human muscle tissues on thin films. On this platform, DMD myoblasts formed fewer and smaller myotubes and exhibited impaired polarization of the cell nucleus and contractile cytoskeleton when compared with healthy cells. These structural aberrations were reflected in their functional behavior, as engineered tongues from DMD myoblasts failed to achieve the same contractile strength as healthy tongue structures. These data suggest that dystrophic muscle may fail to organize with respect to extracellular cues necessary to potentiate adaptive growth and remodeling.

Introduction

Duchenne muscular dystrophy (DMD) is a progressive muscle-wasting disease that occurs in childhood and results in early death. Improvements in clinical management (Bushby et al., 2010; Schram et al., 2013) have lengthened the life span of DMD patients despite the present lack of an etiologic therapy. As patients live longer, management of late-stage clinical manifestations such as dysphagia (Umemoto et al., 2012; Hamanaka-Kondoh et al., 2014) has become increasingly important for maintaining quality of life. In DMD, dysphagia occurs during the oral phase of swallowing (van den Engel-Hoek et al., 2013), where tongue weakness causes failed propulsion of food from the oral cavity to the pharynx. The cause of tongue weakness, like all muscle weakness in DMD, is the failure of muscle stem cells to repair damaged muscle, which is instead replaced with fibrofatty tissue.

We reasoned that muscular repair in the tongue proceeds in the same manner as in other muscles: satellite cells proliferate and differentiate into myoblasts, which align with the underlying ECM, elongate, and fuse to form nascent myotubes (Standish and Eversole, 1970; Noden, 1986; Webster et al., 2016). In DMD, loss-of-function mutations to dystrophin cause impairment of satellite cell division (Dumont et al., 2015) and degrade the structural integrity of skeletal muscle cells (Pasternak et al., 1995). However, whether dystrophin deficiency affects myoblasts and the role of ECM cues in fusion and myofibrillogenesis processes is still largely unknown. A study comparing myoblasts derived from young and old *mdx* mice (Alexakis et al., 2007), a murine model of DMD, found that fewer cells from old-aged *mdx* muscle exhibited myogenic markers and instead had increased expression of collagen type I. The disparate expression profile of myogenic markers between young and old *mdx* mice suggests DMD myoblasts may have reduced potential to proceed through myogenesis because of the acquisition of a fibrotic phenotype.

In this report, we introduce a tongue-inspired in vitro platform for the study of muscle formation and function using myoblasts from healthy and DMD patients. The film bending elicited by muscle contraction on our cantilevered design (Grosberg et al., 2011a) mimics the tongue bending that occurs during swallowing, where the superior muscle layer contracts more than the inferior muscle layers (Napadow et al., 2002), producing a bending motion. We hypothesized that DMD myoblasts are less sensitive to cues in the ECM designed to potentiate the structure–function relationships of healthy muscle. To test this hypothesis, we analyzed the cytoskeletal and nuclear alignment of healthy or DMD myoblasts seeded onto an array of narrowly spaced ECM bands patterned on our engineered tongue on a chip. We found that the cytoskeleton (CSK) and

The Rockefeller University Press $30.00
J. Cell Biol. Vol. 215 No. 1   47–56
www.jcb.org/cgi/doi/10.1083/jcb.201603111

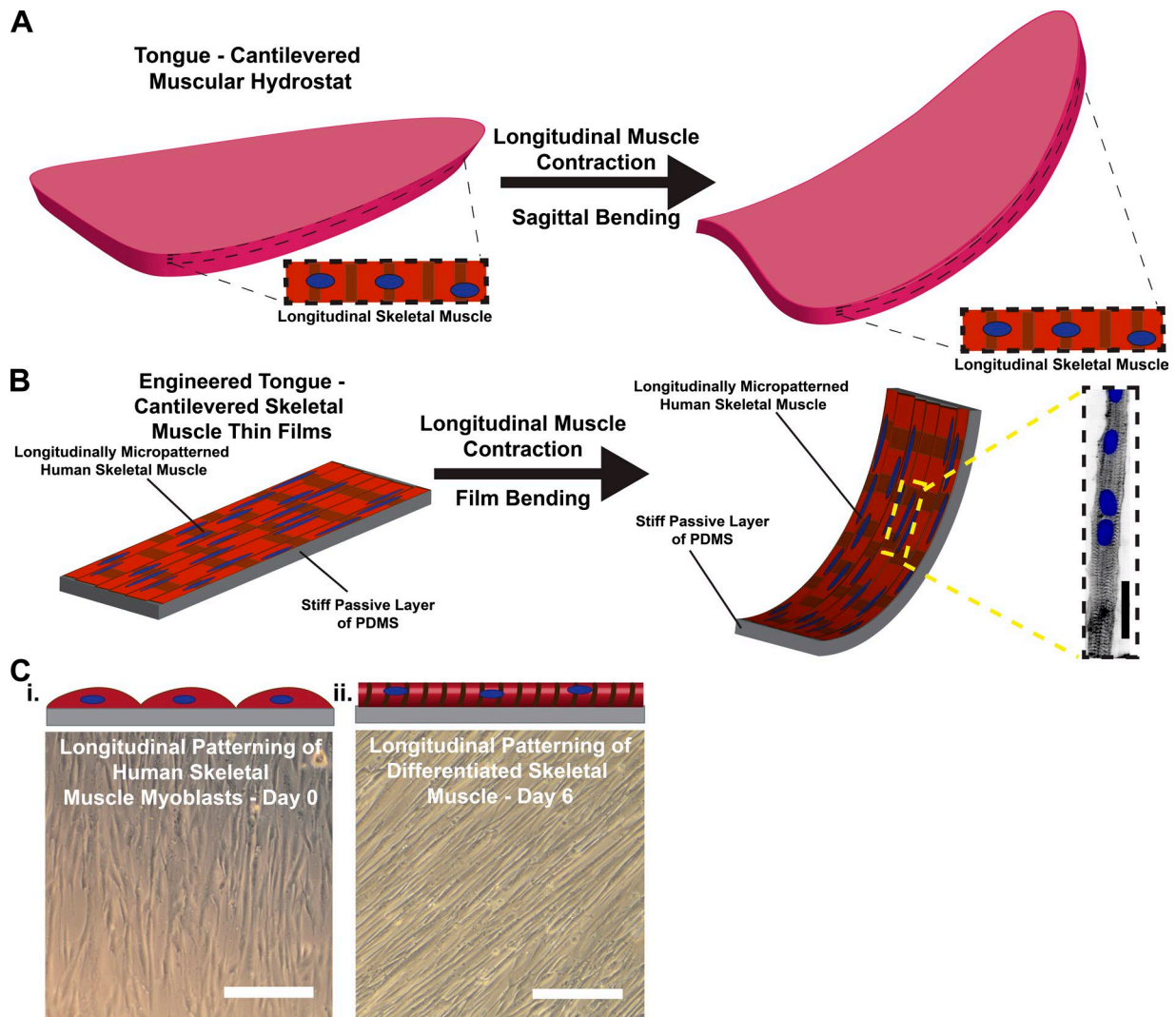JCB   47

THE JOURNAL OF CELL BIOLOGY

Figure 1. **Designing the tongue on a chip.** (A) Schematic representation of tongue bending caused by contraction of a longitudinal skeletal muscle. (B) Schematic representation of the tongue on a chip. Immunostaining shows myotubes cultured on PDMS film in the magnified section (SAA, black; nuclei, blue). Bar, 50 µm. (C) Representative tissue culture images of myoblasts (i) and differentiated skeletal muscle (ii). Bars, 100 µm.

nuclei of DMD myoblasts failed to polarize to the same degree as healthy tissues. These structural differences yielded fewer and smaller myotubes in DMD tissues. Furthermore, comparison of contractile function of healthy and DMD tissues revealed profound contractile weakness in DMD engineered tongues. These data suggest that impaired polarization with respect to the underlying ECM observed in DMD myoblasts may prevent the muscular repair necessary to potentiate strong and efficient contractile function of healthy muscle.

Results and discussion

Developing a tongue on a chip
Tongues are muscular hydrostats whose movements are facilitated by a complex, multilayer architecture (Wedeen et al., 2001) where the superior extrinsic muscles align parallel to the longitudinal axis of the tongue (Fig. 1 A) and the intrinsic muscles of the tongue orient orthogonally to the tongue surface. The sagittal tongue bending that occurs during swallowing is achieved by contraction of the superior longitudinal muscle and

antagonistic contraction of the intrinsic muscular core, which prevents shortening of the longitudinal muscle (Kier and Smith, 1985) and instead causes bending (Fig. 1 A). Here, we took inspiration from the bending motion of the tongue to engineer laminar anisotropic muscles on stiff but elastic thin films that bend, rather than shorten, upon muscle contraction (Fig. 1 B). We refer to this bio-inspired platform as tongue on a chip because the contractile measurements obtained using this platform can serve as a strength assessment test analogous to measurements of tongue strength performed clinically that quantify the pressure generated during sagittal bending against the palate of the mouth (Umemoto et al., 2012; Hamanaka-Kondoh et al., 2014).

DMD myoblasts exhibit decreased CSK and nuclear anisotropy
We engineered the tongue chips with human myoblasts from healthy or DMD patients. An inherit limitation of primary cell sources is the variability within the host muscle microenvironment. To minimize differences in host muscle microenvironments such as fibrosis in DMD muscle, myoblasts derived from a 2-yr-old DMD patient were used, an age that typically
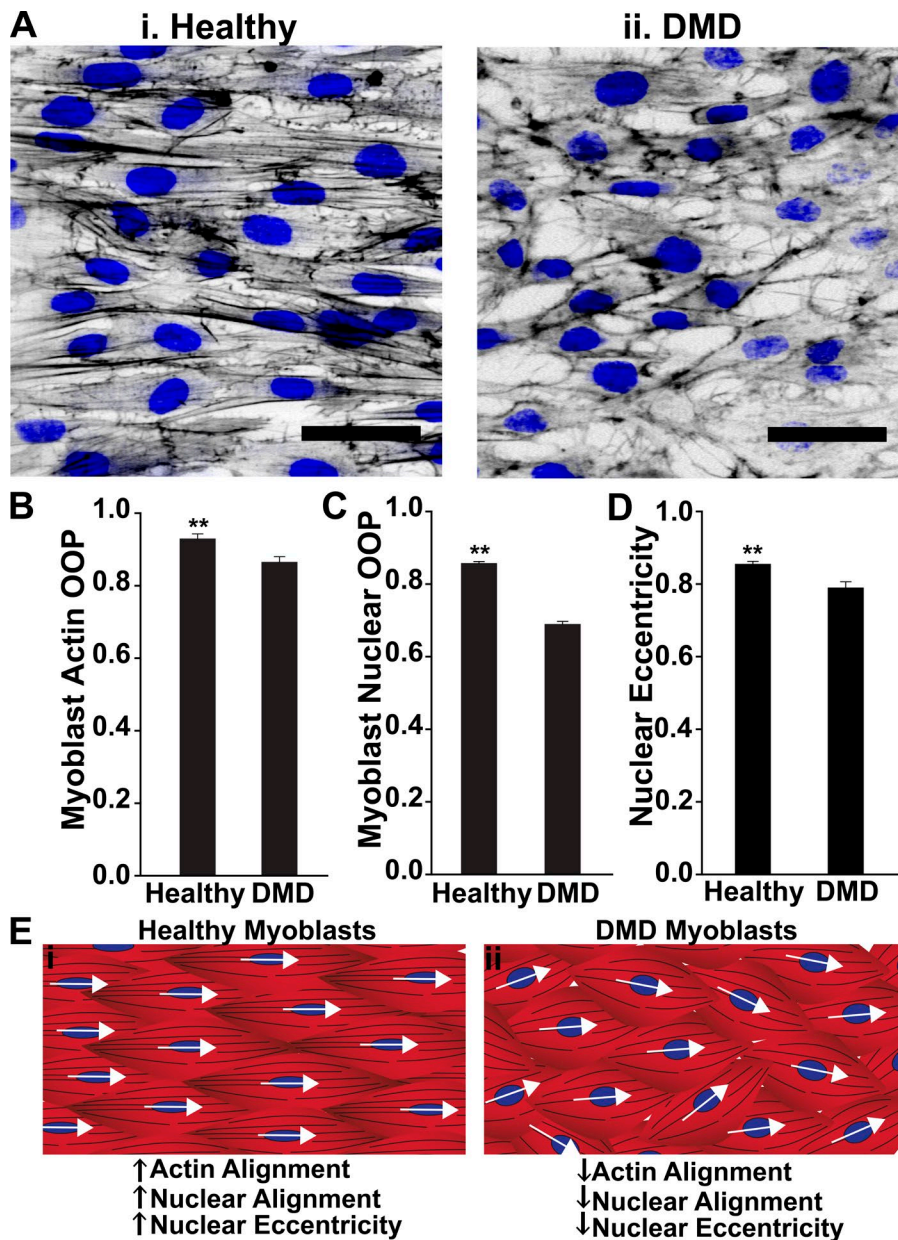
Figure 2. DMD myoblasts exhibit decreased cytoskeletal and nuclear anisotropy. (A) Representative healthy (i) and DMD (ii) myoblast tissues immunostained for f-actin (black) and nuclei (blue). Bars, 50 µm. (B) Actin OOP is plotted. $n = 5$ coverslips, 10 FOVs per sample for each condition. (C) Myoblast nuclear OOP is plotted. (D) Myoblast nuclear eccentricity is plotted. (C and D) $n = 5$ coverslips, 3 FOVs per sample, >700 nuclei analyzed for each condition. (E) Schematic representations of healthy (i) and DMD (ii) myoblasts and a summary of results. Black lines represent actin fibrils. White arrows represent orientation of the nuclei (blue). For all data in this figure, **, $P < 0.05$. All FOVs were 318.5 × 318.5 µm. Error bars represent mean ± SEM.

precedes clinical symptoms (Biggar, 2006). Western blot studies confirmed expression of myogenin in healthy and DMD tissues, indicating the myoblasts had maintained a myogenic phenotype (Fig. S1 A); however, contributions of distinct host microenvironments cannot be entirely eliminated in the interpretation of the data in this report.

In vivo, myoblast migration and polarization are guided by ghost fibers left behind by damaged myofibers promoting myotube formation (Webster et al., 2016). Fibronectin (FN; Lukjanenko et al., 2016) and merosin (M; Sanes, 2003) have been identified as critical ECM proteins within the muscle stem cell niche for muscle regeneration. We hypothesized that DMD myoblasts are less sensitive to cues in the ECM that guide the alignment and polarization requisite for myotube formation. To test this hypothesis, FN, M, or a mixture of FN and M (FNM) was microcontact printed in an array of narrowly spaced bands and seeded with myoblasts. Myoblasts were cultured in growth media to allow for formation of a confluent tissue (day 0 [D0]). Immunohistochemistry was used to identify the

actin CSK and nuclei within the tissues (Fig. 2 A, i and ii). The alignment of the actin CSK was quantified by calculating the orientational order parameter (OOP; Grosberg et al., 2011b), a score of global anisotropy ranging from zero to one, representing random and parallel alignment, respectively. The actin CSK of the DMD myoblast tissues was less aligned compared with the healthy myoblast tissues cultured on FN, M, and FNM (Fig. 2 B; Fig. S2, A and D; and Fig. S3, A and D), suggesting DMD myoblasts do not align with the underlying ECM as effectively as healthy controls.

Moreover, polarized cells of larger aspect ratios exhibit nuclei of greater eccentricity (Khatau et al., 2009; Ye et al., 2014) and decreased nuclear offset than cells of smaller aspect ratios (Ye et al., 2014). To quantify nuclear alignment and shape, we used a previously described method that utilizes an ellipse-fitting tool to outline each nucleus within a field of view (FOV; Bray et al., 2010). Nuclear OOP was calculated using the orientations of the major axes of the fitted ellipses. A comparison of the nuclear alignment revealed that DMD myoblast

tissues had decreased nuclear alignment (Fig. 2 C and Figs. S2 E and S3 E) relative to healthy controls regardless of ECM composition. Healthy myoblasts formed organized tissues with high nuclear eccentricity when seeded onto FN and FNM substrates. (Fig. 2 D and Fig. S3 F). Tissues formed on M alone exhibited decreased actin OOP, nuclear OOP, and eccentricity in both healthy and DMD samples (Fig. 2, B–D; Fig. S2, D–F; and Fig S3, D–F). Collectively, these data indicate that DMD myoblasts do not align and polarize in the same manner as healthy myoblasts in response to ECM cues alone.

DMD myotubes form aligned actin CSK but have less eccentric nuclear shapes

Previous studies (McGrath et al., 2003; Nowak et al., 2009) report changes in myoblast morphology from fibroblast-like to an elongated, bipolar morphology in response to switching to a low-serum differentiation medium before fusion. We hypothesized that DMD myoblasts would undergo more significant morphological changes in response to a serum deficit because of decreased polarization in response to ECM cues alone. To test this hypothesis, we assessed cellular polarization in the presence of media containing high (D0) and low (D3 and D6) amounts of serum by quantifying the actin OOP, nuclear OOP, and nuclear eccentricity (Fig. 3 A; Fig. S2, D–F; and Fig. S3, D–F). In healthy and DMD tissues cultured on FN, the actin alignment increased from D0 to D6, but not in healthy tissues cultured on M or FNM (Fig. 3, A and B; and Figs. S2 D and S3 D). Additionally, a significant increase in nuclear alignment occurred from D0 to D3 and D6 in healthy and DMD tissues cultured on FN and FNM, as well as DMD tissues cultured on M (Figs. 3 C, S2 E, and S3 E). Similarly, nuclear eccentricity increased from D0 to D6 in healthy and DMD tissues cultured on FN or FNM (Figs. 3 D and S3 F) but not on M (Fig. S2 F). The relatively large increase in nuclear alignment and eccentricity in DMD tissues from D0 to D3 is consistent with the morphological changes observed in myoblasts before fusion (Fortier et al., 2008), whereas healthy myoblasts on FN and FNM exhibited highly aligned and eccentric nuclei on D0 due to the ECM patterning alone. Collectively, these data suggest that myoblasts align their actin CSK and nuclei in parallel with the underlying ECM before fusion; however, DMD myoblasts require additional cues, such as deficits in growth factors, to achieve the alignment and polarization observed in healthy tissues.

DMD myoblasts form fewer, smaller, and more immature myotubes

Myoblasts deficient of RhoE were shown to exhibit poor alignment and elongation, similar to DMD myoblasts before switching to a low-serum differentiation media, that resulted in the failure of myotube formation (Fortier et al., 2008). We asked whether the decreased and delayed polarization observed in DMD tissues in the present study would result in decreased myotube formation as well. To answer this question, we quantified myotube density by counting the number of myotubes expressing sarcomeric α-actinin (SAA) per FOV. We found that healthy tissues had a greater density of myotubes on D3 and D6 compared with DMD tissues (Fig. 4, A and B; and Figs. S2 H and S3 H). Moreover, we used Western blot to compare the expression of M-cadherin, which localizes at the cell-to-cell junction of fusing myoblasts (Zeschnigk et al., 1995). Consistent with the measurements of myotube density, healthy tissues had greater M-cadherin expression on D0 before induction of

differentiation compared with DMD tissues and continued to have greater expression on D1–4 (Fig. S1 B). Comparison of mean myotube diameter revealed that healthy myotubes cultured on FN had significantly larger diameters relative to DMD myotubes (Fig. 4, A and C), but mean healthy myotube diameter was decreased in tissues cultured on M and FNM compared with FN (Figs. S2 I and S3 I).

In addition to remodeling cellular architecture during myoblast fusion, fused myoblasts undergo myofibrillogenesis. In brief, premyofibrils form at the edges of the myotube in the form of Z bodies, which are rich in punctate SAA. Over time, these Z bodies fuse to form Z disks that represent the boundaries of the contractile unit called sarcomeres (Dabiri et al., 1997). We asked whether the slower alignment of DMD myoblast tissues resulted in delayed myofibrillogenesis. To answer this question, the abundance and ordered structure of the SAA of healthy and DMD engineered muscle were quantified. The abundance of SAA was measured by quantifying the projected area of the SAA immunosignal relative to the area of f-actin immunosignal on D3 and D6. On D3 in healthy tissues cultured on FN and FNM, myotubes had significant expression of SAA, whereas very little SAA expression was observed in the DMD tissues on any ECM and healthy tissues on M (Fig. 4, A and D; and Figs. S2 G and S3 G). Furthermore, we observed a greater projected area of SAA immunosignals in the healthy condition compared with the DMD condition on D6 (Fig. 4, A and D; and Figs. S2 G and S3 G), indicating healthy tissues were at a later stage of myogenesis compared with DMD tissues. To determine whether Z bodies were undergoing organized assembly into Z disks, we quantified the fraction of periodically distributed SAA immunosignals, termed sarcomeric packing density (SPD; Pasqualini et al., 2015). Healthy tissues had significantly greater SPDs compared with DMD tissues on D6 (Fig. 4 E). The SAA immunosignal was not significant enough in the DMD condition on D3 to compare statistically with the healthy condition. The relative lack of SAA and SAA organization observed in the DMD tissues at these time points is likely, in part, caused by the delayed fusion in these tissues, not dystrophin deficiency alone. Collectively, these data indicate that DMD myoblasts form myotubes and undergo myofibrillogenesis, but these processes are delayed relative to healthy tissues. Moreover, these data, in conjunction with previous studies (Lakonishok et al., 1992; García et al., 1999; Mayer, 2003), suggest that $\alpha_5\beta_1$-integrin binding to FN during muscle regeneration may serve as a transient, developmental anchor to the ECM before forming robust focal adhesions through the $\alpha_7\beta_1$-integrin and the dystroglycan complex binding to M in stronger, mature muscle.

Engineered DMD tissues exhibit contractile weakness

The majority of force transmission from sarcomeres propagates laterally through the CSK to integrin-associated and dystroglycan complexes in the sarcolemma to the ECM (Street, 1983; Huijing, 2003; Rahimov and Kunkel, 2013). We hypothesized that engineered tissues from DMD myoblasts would contract significantly less than healthy tissues because of the absence of dystrophin as well as the relative structural immaturity observed in DMD tissues. When engineered tissues were stimulated with an increasing frequency of electrical stimulation, contractile strength increased, causing film bending. Using a high-speed camera, we acquired videos of film bending and used a geometrical relation to calculate the change in the radius
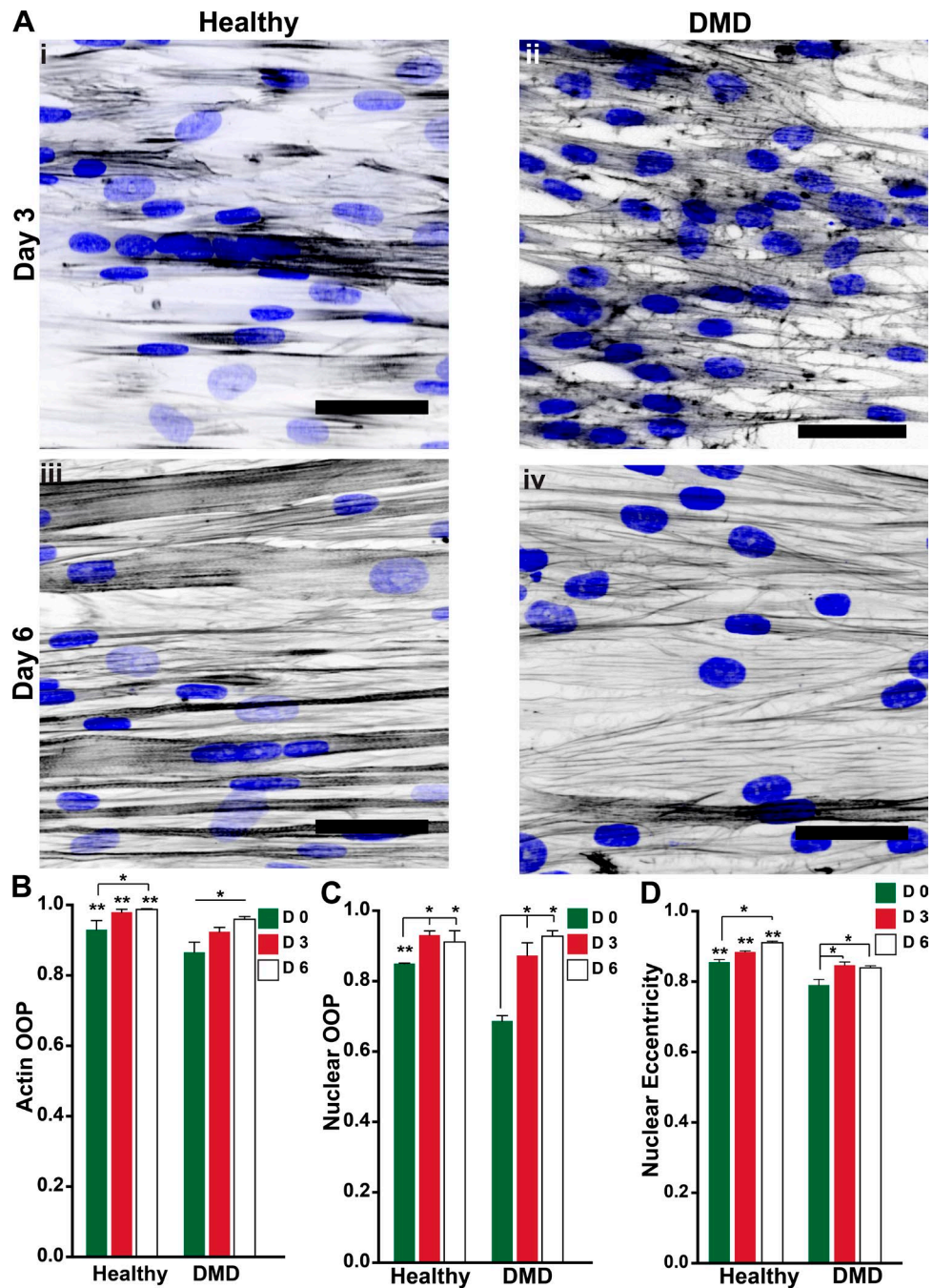
Figure 3. **DMD myotubes form highly aligned actin CSK but have less eccentric nuclear shape.** (A) Representative images of D3 (i and ii) and D6 (iii and iv) healthy (i and iii) and DMD tissues (ii and iv) immunostained for f-actin (black) and nuclei (blue). Bars, 50 μm. (B) Actin OOP is plotted. n = 5 coverslips, 10 FOVs per sample, for each condition. (C) Nuclear OOP is plotted. n = 5 coverslips, 3 FOVs per sample, >400 nuclei analyzed for each day, for each condition. (D) Nuclear eccentricity is plotted. n = 5 coverslips, 3 FOVs per sample, >400 nuclei analyzed for each condition. For all data in this figure, *, $P < 0.05$ relative to other days within a condition; **, $P < 0.05$ relative to the other condition on the corresponding day. All FOVs were 318.5 × 318.5 μm. Error bars represent the mean ± SEM.

of curvature (Grosberg et al., 2011a). The change in the radius of curvature, the film thickness, and the material properties of the polydimethylsiloxane (PDMS) film were imputed into the growth theory–based model used to calculate contractile stress (Alford et al., 2010).

To compare the relative contractile strength of the healthy and DMD tissues, baseline stress, peak stress, and dynamic stress were quantified (Fig. 5, A and B). DMD tissues had lower baseline stress on both D3 and D6 compared with healthy tissues (Fig. 5 D). Similarly, DMD tissues had weaker peak stress compared with healthy tissues on D6 (Fig. 5 E). However, no observable contractions were obtained from DMD tissues on D3, so a comparison of peak stress was not included for this time point. Lastly, in both conditions, we observed increases in dynamic stress as stimulation frequency was increased (Fig. 5 F), but no observable contractions were obtained in DMD tissues when stimulated at frequencies ranging from 1 to 4 Hz on D6. Healthy tissues had at least
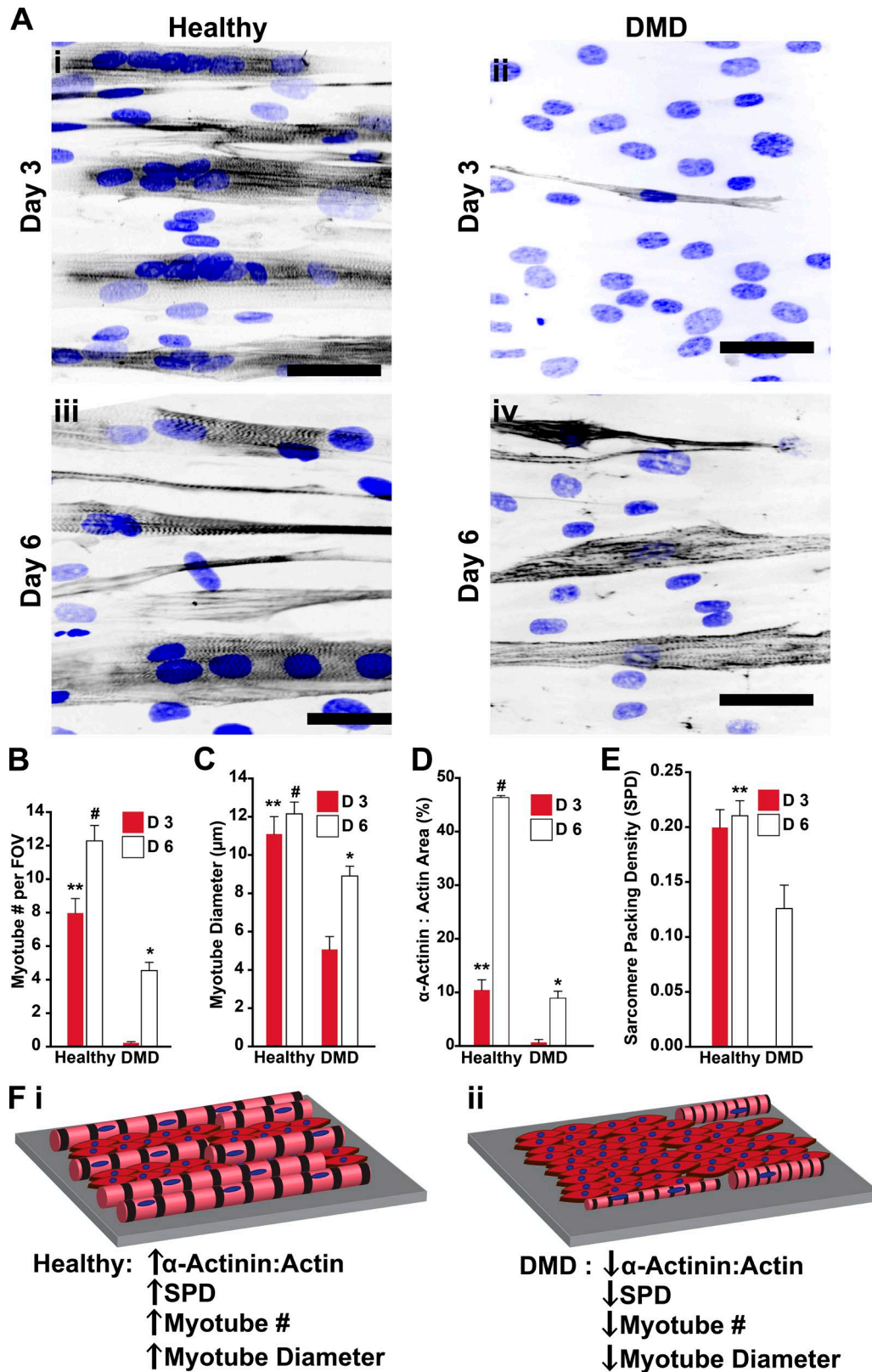
Figure 4. **DMD myoblasts form fewer, smaller, and more immature myotubes.** (A) Representative D3 healthy and DMD tissues (i and ii) and D6 healthy and DMD tissues (iii and iv) immunostained for SAA (black) and nuclei (blue). Bars, 50 µm. (B) Myotube density is plotted. (C) Myotube diameter is plotted. (D) The SAA/actin area ratio is plotted for D3 and D6. (E) SPD is plotted. The D3 DMD condition did not have significant enough SAA expression for statistical comparison. (F) Schematic representation of healthy (i) and DMD (ii) tissues and a summary of results. Unfused myoblasts are represented in red, and fused myotubes are represented in pink. For all data in this figure, $n = 5$ coverslips, 10 FOVs (318.5×318.5 µm) per sample, for each condition, for each day. *, $P < 0.05$ relative to D3 within a condition; **, $P < 0.05$ relative to the DMD condition on the corresponding day; #, $P < 0.05$ relative to the other day within a condition and to the other condition on the corresponding day. Error bars represent mean ± SEM.
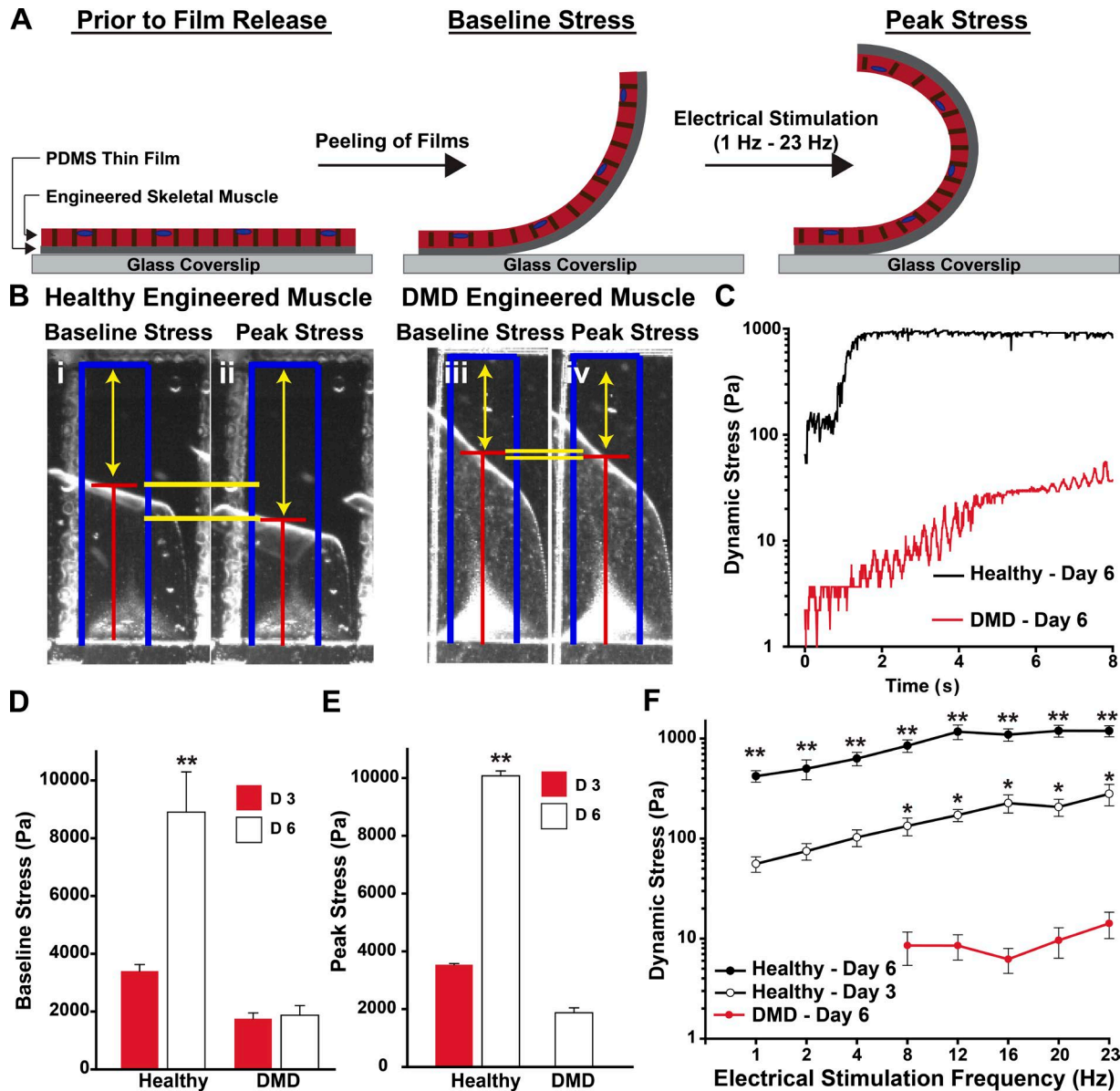
Figure 5. **DMD tissues exhibit contractile weakness.** (A) Schematic representation of tissues before film release, at baseline stress, and at peak stress. (B) Representative images of healthy (i and ii) and DMD (iii and iv) tissues at baseline (i and iii) and peak stress (ii and iv). Blue rectangles represent film length. The red bar represents the tracking of the film edge. The yellow arrows represent the distance between the projected film length and the unstressed film length. The yellow bars represent the change in projected film length from baseline stress (top bar) to peak stress (bottom bar). (C) Representative stress trace of a healthy and DMD contraction in response to 23-Hz stimulation. $n = 1$ film for each condition. (D) Baseline stress is plotted for the healthy and DMD conditions on D3 and D6. (E) Peak stress is plotted for the healthy condition on D3 and D6 and the DMD condition on D6. For the DMD condition, no contraction was observed on D3. (F) Dynamic stress is plotted for the healthy condition on D3 and D6 and the DMD condition on D6. For the DMD condition, no contraction was observed on D3. Data points represent the mean ± SEM. For all stress measurements (D–F): for the healthy D3 condition, $n = 11$ films, 3 chips; for the healthy D6 condition, $n = 10$ films, 3 chips; for the DMD D3 condition, $n = 12$ films, 2 chips; for the DMD D6 condition, $n = 14$ films, 3 chips. **, $P < 0.05$ relative to both conditions on either day. *, $P < 0.05$ relative to the DMD condition on D6. Error bars represent median ± SEM.

one order of magnitude greater dynamic stress on D3 and D6 relative to the D6 DMD tissues at all stimulation frequencies (Fig. 5 F). The large differences in dynamic stress could result from the structural immaturity, dystrophin deficiency, or a combination of the two, but these factors cannot be decoupled at these time points. Together, these data quantify contractile weakness in engineered human dystrophic skeletal muscle in vitro. Hence, we have demonstrated that we can recapitulate aspects of both the decreased muscle regeneration and the muscle weakness observed in DMD patients using a human in vitro model.

In this study, we demonstrate the maladaptive functional consequences of the failure of self-assembly of DMD myoblasts during multiple stages of myogenesis. DMD myoblasts failed to self-organize their actin CSK and nuclei in the same manner as healthy myoblasts in response to ECM cues. These structural aberrations led to impaired myotube assembly in DMD tissues, reflected by the reduced density and size of myotubes. Moreover, self-assembly of the contractile apparatus in DMD tissues was reduced and disordered compared with healthy tissues. Collectively, these structural deficits were reflected by severe contractile weakness in DMD tissues. These insights may

explain, in part, how the incomplete repair of muscle results in profound muscle weakness in DMD.

Materials and methods

Tongue chip fabrication

Glass coverslips (VWR) were placed vertically within a metal rack for cleaning via immersion into 70% ethanol, followed by 30 min of sonication. After allowing for drying, a low-adhesive tape (5560; Patco) was applied to cover the entire surface of the coverslip. Next, a single rectangular island (9 × 5.5 mm) was laser engraved into the tape using a CO_2 laser (Epilog). After removing the rectangular island, leaving the remainder of the coverslip masked, a thin layer of the thermally sensitive polymer, poly(*N*-isopropylacrylamide) (PIPAAm; Polysciences) dissolved in 1-butanol (10% wt/vol), was spin coated on the exposed glass region of the chip, using a maximum rotational speed of 6,000 rpm. After removal of the remaining tape, PDMS (Sylgard 184; Dow Corning) was mixed at a 10:1 base to curing agent weight ratio and spin coated at a maximum speed of 4,000 rpm for 1 min such that a thin, uniform layer of PDMS coated both the entire coverslip surface as well as the thin layer of PIPAAm. Subsequently, the chips were allowed to cure overnight at 65°C. Next, an array of 4 to 6 cantilevers (2 mm wide and 5 mm long) was laser engraved into the polymer layers. Subsequently, the tongue chips were washed vigorously in sterile, 37°C PBS.

Human skeletal muscle culture

Human skeletal muscle myoblasts (Lonza) were purchased and cultured in a growth media consisting of M199 culture media (Gibco) supplemented with 10% heat-inactivated fetal bovine serum, 10 mM Hepes, 0.1 mM MEM nonessential amino acids, 20 mM glucose, 1.5 μM vitamin B-12, and 50 U·ml^{-1} penicillin (Gibco). The myoblasts derived from a DMD patient were purchased from DV Biologics and were cultured in the same growth media. Cells were plated and expanded in T-75 culture flasks (Corning) before cell seeding. Before cell plating, T-75 culture flasks were incubated with 1% wt gelatin from porcine skin (Sigma-Aldrich) in a cell culture incubator for 30 min. The 1% gelatin solution was subsequently replaced with growth media in preparation for cell plating. The skeletal muscle myoblasts were allowed to proliferate over the course of 2–3 d and were seeded before reaching 70% confluence. Cell culture media was replenished after 48 h after three rinses with sterile PBS. For myoblast seeding, cells were removed from the cell culture flask using 0.25% of trypsin-EDTA (Gibco) and seeded onto chips at a density of 62,000 cells·cm^{-2}. The myoblasts formed confluent monolayers of tissue after 2 d in growth media when cultured on either FN or FNM. On M, healthy and DMD myoblasts formed confluent tissues after 5 d in growth media. Next, to induce differentiation of the myoblasts, the growth media was replaced with a differentiation media consisting of DMEM-F12 (Lonza), supplemented with 2% horse serum (Gibco). Differentiation media was replenished every 48 h. Experiments were performed during a period ranging from 3 d of culture in differentiation media to 6 d of culture in differentiation media.

Microcontact printing

To direct anisotropic tissue formation along the longitudinal axis of the muscular thin film, FN, M, or FNM was microcontact printed in a geometrical pattern of an array of 15-μm bands, with 2-μm spacing, using a previously published method (Chen et al., 1997; Alford et al., 2011). In brief, a silicone stamp with a defined geometrical pattern on one surface was fabricated by first fabricating a negative replica on a silicon wafer using photolithography. The silicon wafer (76-mm diameter) was

coated with a layer of the negative photoresist, SU8-2002 (MicroChem Corporation), using spin coating. After baking the photoresist-coated silicon wafer, a chrome photomask was carefully applied to the surface of the photoresist-coated wafer using a mask aligner, and UV light was shown through the mask for 7–10 s. Subsequently, the regions not exposed to UV light were washed away using a development solution, and curing was completed by a final baking step at a maximum temperature of 180°C for 30 min. This etched wafer serves as a negative template for the silicone stamp. PDMS was poured over the template and degassed. The PDMS was allowed to cure overnight at 65°C. Next, the PDMS was carefully removed from the etched silicon wafer and was cut into individual rectangular stamps for application to single coverslips. To transfer a defined pattern of ECM onto the tongue chips, the PDMS stamps were coated and subsequently incubated with human FN (BD), human M (Sigma-Aldrich), or an equimass mixture of FNM at 50 μg·ml^{-1} in sterile, distilled water for 1 h. Next, excess ECM protein was removed from the PDMS stamp using compressed air, and the PDMS stamp was carefully applied to the muscular thin film chip, which had been recently exposed to UV ozone (342; Jetlight Company Inc.) for 8 min to transiently functionalize the surface for protein binding. After removal of the PDMS stamp, the chips were rinsed with PBS and promptly seeded with cells.

Immunohistochemistry

Engineered human skeletal muscle tissues were fixed by treatment with 4% (vol/vol) paraformaldehyde for 15 min (16% stock diluted in PBS; Electron Microscopy Sciences) and permeabilized with 0.05% (vol/vol) Triton X-100 in PBS at room temperature for 5 min. The samples were then washed with PBS before incubation with primary antibodies. The samples were incubated with a primary antibody solution consisting of a 1:200 dilution of monoclonal anti-SAA antibodies (A7811; clone EA-53; Sigma-Aldrich) in PBS for 2 h at room temperature. After rinsing three times with room temperature PBS, the engineered tissues were incubated with a secondary solution consisting of 1:200 dilutions of Alexa Fluor 546–conjugated goat anti–mouse IgG secondary antibody (Invitrogen), Alexa Fluor 488–conjugated phalloidin (A12379; Invitrogen), and DAPI (D1306; Invitrogen) for 1 h at room temperature. Fluorescence microscopy was performed using a laser-scanning confocal microscope (ZEISS) using the enhanced contrast Plan-Neofluar 40×/1.3 oil differential interference contrast M27 objective at room temperature.

Quantitative analysis of nuclear architecture

Nuclear eccentricity and orientation were quantified using a custom MATLAB software (MathWorks) developed in our group and described previously (Bray et al., 2010). In brief, an ellipse-fitting algorithm was used to trace the perimeter of nuclei in immunofluorescence images, enabling measurement of major and minor axes lengths and eccentricity. To measure orientation angle, an orientation vector was drawn through the longitudinal axis of the fitted ellipse. To quantify global nuclear alignment, the OOP was calculated using the mean resultant vector of the measured orientation angles from circular statistics (Berens, 2009). Measurements were repeated for every nucleus within an FOV, excluding overlapping nuclei as well as nuclei not fully within the FOV. Statistical analyses to compare nuclear data were performed using SigmaPlot 12.0 software (Systat). Data from each condition were analyzed using two-way analysis of variance and compared pairwise using the Holm-Sidak method. Results with p-values of <0.05 were considered statistically significant.

Quantitative analysis of actin CSK and sarcomere organization

We used custom image analysis software developed in our group and published previously (Pasqualini et al., 2015) to analyze the

organization of the actin CSK and sarcomeres. In brief, for analysis of the actin CSK, the orientation of actin fibers was determined using the OrientationJ plugin (Rezakhaniha et al., 2012), and the actin OOP was calculated for each sample. The global OOP was calculated for each sample by analyzing 10 FOVs (318.5 × 318.5 µm). Five samples were compared for each condition on each day of comparison. Statistical analysis was performed using SigmaPlot 12.0 software. Data from each condition were analyzed using a two-way analysis of variance and compared pairwise using the Holm-Sidak method. Results with p-values of <0.05 were considered statistically significant.

To quantify the expression of SAA, we measured the projected area of the pixels positive for SAA immunosignal relative to the projected area of the pixels positive for phalloidin immunosignal using custom MATLAB software. To determine the relative presence of sarcomeres as periodic structures in the SAA stainings, we used a previously published method from our group (Pasqualini et al., 2015). In brief, the 2D Fourier transform of the SAA immunostaining was radially integrated in a 1D signal that contains the relative importance of each spatial frequency. This signal was then fitted to separate the aperiodic contribution of the Z bodies from the periodic contribution of the Z disks. The ratio of the areas under the periodic and aperiodic components, named the SPD, was used to compare the relative assembly of sarcomeres among the conditions.

Myotube density was quantified by counting the number of myotubes per FOV for 10 FOVs, for five coverslips, for each condition on D3 and D6. The myotube diameter was quantified by measuring the projected cross-sectional diameter of each myotube in each FOV using ImageJ (National Institutes of Health). The mean myotube density and diameter were calculated for each sample. The means of five coverslips were compared using a two-way analysis of variance and compared pairwise using the Holm-Sidak method. Results with p-values of <0.05 were considered statistically significant.

Muscular thin film contractility measurements

For contractility experiments, the tongue chips were transferred to a 60-mm Petri dish containing normal Tyrode's solution (1.8 mM $CaCl_2$, 5 mM glucose, 5 mM Hepes, 1 mM $MgCl_2$, 5.4 mM KCl, 135 mM NaCl, and 0.33 mM NaH_2PO_4 in deionized water, pH 7.4, at 37°C; Sigma-Aldrich). Field stimulation electrodes made of 1-mm platinum wire (VWR) were built into an acrylic lid and fitted on to the 35-mm Petri dish. Contraction of the skeletal muscle was induced using an external field stimulator (Myopacer; IonOptix Corp.), which applied field stimulation over a range of frequencies spanning from 1 to 23 Hz, with an amplitude of 10 V. The horizontal projection of film bending was captured using a stereomicroscope (Leica MZ9.5; Wetzlar) with 0.63× magnification, which was coupled to a data acquisition board (LabVIEW; National Instruments) programmed to capture the experiment using a camera (Basler A601f-2; Exton) at a frame rate of 100 frames per second. Contractile stress quantification was performed using a previously published method from our group (Alford et al., 2010; Grosberg et al., 2011a). In brief, the change in radius of curvature was measured by first thresholding each frame of the videos of the contractile experiments to measure the projection length of each film using a custom macro ImageJ software that has been previously described (Grosberg et al., 2011a). MATLAB software was used to then calculate the film stress using the film projection length from each frame, the film thickness, and the PDMS material properties. The film thickness was measured using a contact profilometer (Dektak 6M; Veeco Instruments Inc.). Baseline stress was measured as the stress within the engineered muscle at rest, before electrical stimulation. Peak stress was measured as the stress at maximum contraction. Dynamic stress was calculated as the difference between the baseline and peak stresses, representative of the contractile stress induced by electrical stimulation (Fig. 5, A–C). Statistical analysis was performed using SigmaPlot 12.0 software. Data from each condition were analyzed using the Mann-Whitney rank sum test for the baseline stress and dynamic stress and using the t test for peak stresses. Results with p-values of <0.05 were considered statistically significant.

Western blot protein analysis

Protein was isolated from engineered human skeletal muscle tissue by lysing cells at 4°C in radioimmunoprecipitation assay lysis buffer (Sigma-Aldrich) plus Complete Mini (Roche). A capillary-based Wes Simple Western Analysis (ProteinSimple) was used to quantify protein expression levels according to the manufacturer's protocol. In brief, 0.5 µg lysate samples was loaded into each capillary, and proteins were separated by size in the separation matrix. Target skeletal muscle differentiation proteins were identified with the following primary antibodies: myogenin (sc576; Santa Cruz Biotechnology, Inc.), M-cadherin (sc274093; Santa Cruz Biotechnology, Inc.), and fast myosin heavy chain (M4276; Sigma-Aldrich). An α-tubulin antibody (ab7291; Abcam) was used as a loading control to normalize expression levels in each sample. The proteins were immunoprobed using mouse and rabbit secondary antibodies and chemiluminescent substrates provided by the manufacturer. Chemiluminescent signals were detected and quantified using Compass Software (ProteinSimple). Data were analyzed using a two-way analysis of variance and compared pairwise using the Holm-Sidak method. Results with p-values of <0.05 were considered statistically significant.

Online supplemental material

Fig. S1 shows that healthy tissues exhibit greater expression of M-cadherin during early differentiation. Fig. S2 shows that healthy and DMD myoblasts have decreased alignment of actin CSKs and nuclei and form fewer myotubes when cultured on anisotropically micropatterned M. Fig. S3 shows that healthy and DMD tissues align and form myotubes similarly when cultured on an anisotropically micropatterned mixture of FNM as compared with FN alone. Video 1 shows sample contraction of healthy engineered tissues electrically stimulated at 23 Hz, visualized using a stereomicroscope and recorded using a Basler A601f-2 camera at 100 frames per second. Videos 2 and 3 show sample contractions of DMD engineered tissues electrically stimulated at 23 Hz, visualized using a stereomicroscope and recorded using a Basler A601f-2 camera at 100 frames per second. Video 3 is a version of Video 2 that displays the video as though captured at 25 frames per second to better facilitate observation of the slower and weaker contraction relative to the healthy controls.

References

Alexakis, C., T. Partridge, and G. Bou-Gharios. 2007. Implication of the satellite cell in dystrophic muscle fibrosis: a self-perpetuating mechanism of collagen overproduction. *Am. J. Physiol. Cell Physiol.* 293:C661–C669. http://dx.doi.org/10.1152/ajpcell.00061.2007

Alford, P.W., A.W. Feinberg, S.P. Sheehy, and K.K. Parker. 2010. Biohybrid thin films for measuring contractility in engineered cardiovascular muscle. *Biomaterials.* 31:3613–3621. http://dx.doi.org/10.1016/j.biomaterials.2010.01.079

Alford, P.W., A.P. Nesmith, J.N. Seywerd, A. Grosberg, and K.K. Parker. 2011. Vascular smooth muscle contractility depends on cell shape. *Integr. Biol. (Camb.).* 3:1063–1070. http://dx.doi.org/10.1039/c1ib00061f

Berens, P. 2009. Circstat: A Matlab toolbox for circular statistics. *J. Stat. Softw.* 31:1–21. http://dx.doi.org/10.18637/jss.v031.i10

Biggar, W.D. 2006. Duchenne muscular dystrophy. *Pediatr. Rev.* 27:83–88. http://dx.doi.org/10.1542/pir.27-3-83

Bray, M.A., W.J. Adams, N.A. Geisse, A.W. Feinberg, S.P. Sheehy, and K.K. Parker. 2010. Nuclear morphology and deformation in engineered cardiac myocytes and tissues. *Biomaterials.* 31:5143–5150. http://dx.doi.org/10.1016/j.biomaterials.2010.03.028

Bushby, K., R. Finkel, D.J. Birnkrant, L.E. Case, P.R. Clemens, L. Cripe, A. Kaul, K. Kinnett, C. McDonald, S. Pandya, et al. DMD Care Considerations Working Group. 2010. Diagnosis and management of Duchenne muscular dystrophy, part 2: implementation of multidisciplinary care. *Lancet Neurol.* 9:177–189. http://dx.doi.org/10.1016/S1474-4422(09)70272-8

Chen, C.S., M. Mrksich, S. Huang, G.M. Whitesides, and D.E. Ingber. 1997. Geometric control of cell life and death. *Science.* 276:1425–1428. http://dx.doi.org/10.1126/science.276.5317.1425

Dabiri, G.A., K.K. Turnacioglu, J.M. Sanger, and J.W. Sanger. 1997. Myofibrillogenesis visualized in living embryonic cardiomyocytes. *Proc. Natl. Acad. Sci. USA.* 94:9493–9498. http://dx.doi.org/10.1073/pnas.94.17.9493

Dumont, N.A., Y.X. Wang, J. von Maltzahn, A. Pasut, C.F. Bentzinger, C.E. Brun, and M.A. Rudnicki. 2015. Dystrophin expression in muscle stem cells regulates their polarity and asymmetric division. *Nat. Med.* 21:1455–1463. http://dx.doi.org/10.1038/nm.3990

Fortier, M., F. Comunale, J. Kucharczak, A. Blangy, S. Charrasse, and C. Gauthier-Rouvière. 2008. RhoE controls myoblast alignment prior through RhoA and ROCK. *Cell Death Differ.* 15:1221–1231. http://dx.doi.org/10.1038/cdd.2008.34

García, A.J., M.D. Vega, and D. Boettiger. 1999. Modulation of cell proliferation and differentiation through substrate-dependent changes in fibronectin conformation. *Mol. Biol. Cell.* 10:785–798. http://dx.doi.org/10.1091/mbc.10.3.785

Grosberg, A., P.W. Alford, M.L. McCain, and K.K. Parker. 2011a. Ensembles of engineered cardiac tissues for physiological and pharmacological study: heart on a chip. *Lab Chip.* 11:4165–4173. http://dx.doi.org/10.1039/c1lc20557a

Grosberg, A., P.L. Kuo, C.L. Guo, N.A. Geisse, M.A. Bray, W.J. Adams, S.P. Sheehy, and K.K. Parker. 2011b. Self-organization of muscle cell structure and function. *PLOS Comput. Biol.* 7:e1001088. http://dx.doi.org/10.1371/journal.pcbi.1001088

Hamanaka-Kondoh, S., J. Kondoh, K. Tamine, K. Hori, S. Fujiwara, Y. Maeda, T. Matsumura, K. Yasui, H. Fujimura, S. Sakoda, and T. Ono. 2014. Tongue pressure during swallowing is decreased in patients with Duchenne muscular dystrophy. *Neuromuscul. Disord.* 24:474–481. http://dx.doi.org/10.1016/j.nmd.2014.03.003

Huijing, P.A. 2003. Muscular force transmission necessitates a multilevel integrative approach to the analysis of function of skeletal muscle. *Exerc. Sport Sci. Rev.* 31:167–175. http://dx.doi.org/10.1097/00003677-200310000-00003

Khatau, S.B., C.M. Hale, P.J. Stewart-Hutchinson, M.S. Patel, C.L. Stewart, P.C. Searson, D. Hodzic, and D. Wirtz. 2009. A perinuclear actin cap regulates nuclear shape. *Proc. Natl. Acad. Sci. USA.* 106:19017–19022. http://dx.doi.org/10.1073/pnas.0908686106

Kier, W.M., and K.K. Smith. 1985. Tongues, tentacles and trunks - the biomechanics of movement in muscular-hydrostats. *Zool. J. Linn. Soc.* 83:307–324. http://dx.doi.org/10.1111/j.1096-3642.1985.tb01178.x

Lakonishok, M., J. Muschler, and A.F. Horwitz. 1992. The $\alpha_5\beta_1$ integrin associates with a dystrophin-containing lattice during muscle development. *Dev. Biol.* 152:209–220. http://dx.doi.org/10.1016/0012-1606(92)90129-5

Lukjanenko, L., M.J. Jung, N. Hegde, C. Perruisseau-Carrier, E. Migliavacca, M. Rozo, S. Karaz, G. Jacot, M. Schmidt, L. Li, et al. 2016. Loss of fibronectin from the aged stem cell niche affects the regenerative capacity of skeletal muscle in mice. *Nat. Med.* 22:897–905. http://dx.doi.org/10.1038/nm.4126

Mayer, U. 2003. Integrins: redundant or important players in skeletal muscle? *J. Biol. Chem.* 278:14587–14590. http://dx.doi.org/10.1074/jbc.R200022200

McGrath, M.J., C.A. Mitchell, I.D. Coghill, P.A. Robinson, and S. Brown. 2003. Skeletal muscle LIM protein 1 (SLIM1/FHL1) induces $\alpha_5\beta_1$-integrin-dependent myocyte elongation. *Am. J. Physiol. Cell Physiol.* 285:C1513–C1526. http://dx.doi.org/10.1152/ajpcell.00207.2003

Napadow, V.J., R.D. Kamm, and R.J. Gilbert. 2002. A biomechanical model of sagittal tongue bending. *J. Biomech. Eng.* 124:547–556. http://dx.doi.org/10.1115/1.1503794

Noden, D.M. 1986. Patterning of avian craniofacial muscles. *Dev. Biol.* 116:347–356. http://dx.doi.org/10.1016/0012-1606(86)90138-7

Nowak, S.J., P.C. Nahirney, A.K. Hadjantonakis, and M.K. Baylies. 2009. Nap1-mediated actin remodeling is essential for mammalian myoblast fusion. *J. Cell Sci.* 122:3282–3293. http://dx.doi.org/10.1242/jcs.047597

Pasqualini, F.S., S.P. Sheehy, A. Agarwal, Y. Aratyn-Schaus, and K.K. Parker. 2015. Structural phenotyping of stem cell-derived cardiomyocytes. *Stem Cell Rep.* 4:340–347. http://dx.doi.org/10.1016/j.stemcr.2015.01.020

Pasternak, C., S. Wong, and E.L. Elson. 1995. Mechanical function of dystrophin in muscle cells. *J. Cell Biol.* 128:355–361. http://dx.doi.org/10.1083/jcb.128.3.355

Rahimov, F., and L.M. Kunkel. 2013. Cellular and molecular mechanisms underlying muscular dystrophy. *J. Cell Biol.* 201:499–510. http://dx.doi.org/10.1083/jcb.201212142

Rezakhaniha, R., A. Agianniotis, J.T. Schrauwen, A. Griffa, D. Sage, C.V. Bouten, F.N. van de Vosse, M. Unser, and N. Stergiopulos. 2012. Experimental investigation of collagen waviness and orientation in the arterial adventitia using confocal laser scanning microscopy. *Biomech. Model. Mechanobiol.* 11:461–473. http://dx.doi.org/10.1007/s10237-011-0325-z

Sanes, J.R. 2003. The basement membrane/basal lamina of skeletal muscle. *J. Biol. Chem.* 278:12601–12604. http://dx.doi.org/10.1074/jbc.R200027200

Schram, G., A. Fournier, H. Leduc, N. Dahdah, J. Therien, M. Vanasse, and P. Khairy. 2013. All-cause mortality and cardiovascular outcomes with prophylactic steroid therapy in Duchenne muscular dystrophy. *J. Am. Coll. Cardiol.* 61:948–954. http://dx.doi.org/10.1016/j.jacc.2012.12.008

Standish, S.M., and L.R. Eversole. 1970. Regenerative changes in rat tongue muscle following crushing injury. *Oral Surg. Oral Med. Oral Pathol.* 30:87–98. http://dx.doi.org/10.1016/0030-4220(70)90017-4

Street, S.F. 1983. Lateral transmission of tension in frog myofibers: a myofibrillar network and transverse cytoskeletal connections are possible transmitters. *J. Cell. Physiol.* 114:346–364. http://dx.doi.org/10.1002/jcp.1041140314

Umemoto, G., H. Furuya, A. Kitashima, M. Sakai, H. Arahata, and T. Kikuta. 2012. Dysphagia in Duchenne muscular dystrophy versus myotonic dystrophy type 1. *Muscle Nerve.* 46:490–495. http://dx.doi.org/10.1002/mus.23364

van den Engel-Hoek, L., C.E. Erasmus, J.C. Hendriks, A.C. Geurts, W.M. Klein, S. Pillen, L.T. Sie, B.J. de Swart, and I.J. de Groot. 2013. Oral muscles are progressively affected in Duchenne muscular dystrophy: implications for dysphagia treatment. *J. Neurol.* 260:1295–1303. http://dx.doi.org/10.1007/s00415-012-6793-y

Webster, M.T., U. Manor, J. Lippincott-Schwartz, and C.-M. Fan. 2016. intravital imaging reveals ghost fibers as architectural units guiding myogenic progenitors during regeneration. *Cell Stem Cell.* 18:243–252. http://dx.doi.org/10.1016/j.stem.2015.11.005

Wedeen, V.J., T.G. Reese, V.J. Napadow, and R.J. Gilbert. 2001. Demonstration of primary and secondary muscle fiber architecture of the bovine tongue by diffusion tensor magnetic resonance imaging. *Biophys. J.* 80:1024–1028. http://dx.doi.org/10.1016/S0006-3495(01)76081-X

Ye, G.J., Y. Aratyn-Schaus, A.P. Nesmith, F.S. Pasqualini, P.W. Alford, and K.K. Parker. 2014. The contractile strength of vascular smooth muscle myocytes is shape dependent. *Integr. Biol. (Camb.)* 6:152–163. http://dx.doi.org/10.1039/c3ib40230d

Zeschnigk, M., D. Kozian, C. Kuch, M. Schmoll, and A. Starzinski-Powitz. 1995. Involvement of M-cadherin in terminal differentiation of skeletal muscle cells. *J. Cell Sci.* 108:2973–2981.